High-resolution *in vivo* nanoparticle imaging using magnetomotive optical coherence tomography

Amy L. Oldenburg, Wei Luo, Stephen A. Boppart*

Beckman Institute for Advanced Science & Technology, University of Illinois at Urbana-Champaign, 405 N. Mathews Ave., Urbana, IL 61801

ABSTRACT

In vivo imaging of the nanoparticle-tissue interaction reveals processes which aid in the improvement of disease-specific markers. Magnetomotive optical coherence tomography (MM-OCT) may fill this role by imaging magnetic nanoparticles (Fe_3O_4, 20-30nm diameter) similar to those currently used for MRI contrast. This is performed by modulating a small (<20mm) electromagnet during conventional OCT imaging and detecting the induced displacement (magnetomotion) of the nanoparticles. In a recent advance, increased specificity was achieved using a 3-pulse sequence to measure the intrinsic background fluctuation to normalize the magnetomotive signal. In this way ghosting due to physiological and Brownian motion are eliminated.

Silicone tissue phantoms which are both optically and mechanically similar to soft human tissue were used to measure the scaling of the magnetomotive signal with magnetic field strength, local optical scattering efficiency, and magnetic nanoparticle concentration. MM-OCT is sensitive to magnetite nanoparticles at a concentration of 220μg/g (P>.975), with the possibility of detecting even lower concentrations (63μg/g) with minor improvements. The MM-OCT signal exhibits a gentler falloff in depth (~4dB over 0.5mm) than conventional OCT imaging, limited ultimately by shot noise. The performance of MM-OCT was evaluated *in vivo* in a *Xenopus laevis* tadpole exposed to magnetic nanoparticles for 24 hours prior to imaging. Corresponding histology demonstrates the ability to correctly identify regions of high nanoparticle concentration with *in vivo* MM-OCT.

Keywords: optical coherence tomography, contrast agents, magnetism, magnetomotion

1. INTRODUCTION

Optical coherence tomography is a microscopic-scale biomedical imaging modality that provides real-time images typically penetrating a few millimeters into biological tissue.[1] Utilizing low-coherence near-infrared light and interferometry, OCT exploits heterodyning to achieve increased signal-to-noise (SNR) over incoherent microscopic imaging. Because it is non-invasive and easily coupled into fiber endoscopes, OCT has proven useful in the clinic particularly for ophthalmology, cardiology and gastroenterology. Clearly, the availability of molecular markers for OCT would greatly enhance the diagnostic capabilities of this technique. However, since OCT relies on the coherence of the backscattered (return) light, it cannot detect fluorescent or bioluminescent probes typically used in incoherent optical imaging.[2]

There have been a variety of recent studies into novel probes and techniques for providing molecularly-specific imaging with OCT. Some of these techniques are specific to endogenous molecules without the need for the introduction of an endogenous probe. This includes nonlinear optical techniques such as second-harmonic generation OCT,[3] and nonlinear interferometric vibrational imaging.[4,5] It also includes spectroscopic OCT detection of endogenous molecules[6] which has been used to sense molecular species active in the near-infrared such as melanin. However, these techniques are somewhat limited to imaging chemical species that are active within the bandwidth of the probe light being used.

Probes which modify the OCT signal by providing increased scattering or absorption have also been employed. These include protein microspheres encapsulating or layered with scattering nanoparticles,[7] and plasmon-resonant gold structures such as silica core nanoshells[8] and nanocubes.[9] Spectroscopic OCT has been used to detect wavelength-specific changes due to near infrared absorbing dyes.[10,11] Transient or switchable absorption in specific dye molecules has also been explored as a means of contrast.[12,13] However, it should be noted that all of the spectroscopic techniques suffer from degradation in the imaging resolution due to the time-bandwidth nature of OCT imaging. In particular, if a resolution of $\Delta\lambda$ is required to sense the wavelength-specific probe, a loss of imaging resolution of a factor of BW/$\Delta\lambda$ (BW=imaging bandwidth) is observed.

Magnetic probes have been of increasing interest in OCT imaging.[14,15] The ability to externally control the probes after their introduction into tissue is extremely powerful. In magnetomotive OCT (MM-OCT) an external electromagnet is modulated to repeatedly pull and release the nanoparticles. This not only allows for imaging by detecting the small induced displacements, but may permit the probing of the elastic properties of the tissue microenvironment.[16] Magnetic nanoparticles also provide a means of therapy by inducing hyperthermia at the site using a high frequency electomagnet (f>100kHz).[17] Typically a magnetic core consisting of magnetite or maghemite is employed which provides a high magnetic susceptibility (χ~1) and saturation magnetization (M_{sat}). Biological tissues exhibit very small susceptibilities ($|\chi|$<10^{-5}), providing a large contrast mechanism which may be employed to differentiate the nanoparticles from the tissue background. The safety of iron-oxide based nanoparticles has been studied extensively and FDA-approved iron oxide core contrast agents such as Combidex[18] are currently in use as MRI contrast agents. These types of particles are typically taken up by healthy macrophages in the lymphatic and reticuloendothelial systems, and have been shown in MRI studies to allow for differentiation between healthy and abnormal lymph nodes for cancer detection.[19]

2. THEORY

In this section, we describe how an externally-applied magnetic field modifies the OCT signal in the vicinity of a magnetic contrast agent and discuss the practical considerations for design of a magnetomotive contrast OCT system. There are several physical mechanisms by which a magnetic particle exposed to a magnetic field B and spatial field gradient ∇B will produce a change in optical scattering. The flow chart in Fig. 1 illustrates the dominance of various mechanisms depending on the strength of the magnetic field and magnetic properties of the particle. All of these mechanisms have a characteristic time constant that is regulated by the viscoelastic properties of the tissue in which the particle is embedded. The current experiments suggest that we are primarily observing displacement and not rotation; however we will briefly outline how rotation might also be detected in future experiments, which may be particularly useful for nanoparticles that are highly elongated.

2.1. Motive dependence of the OCT signal

The induced movement of a magnetic particle and its surrounding medium will alter the signal detected at the output of a Michelson interferometer employed for OCT imaging. Let us consider a magnetic particle embedded in a medium. The sample is scanned with an OCT imaging beam where the incident light is along the z axis, has a confocal parameter which is large with respect to the particle diameter, and the coherence gate is centered at z_d. The particle is located at $(\vec{r}_p, z_p)$ such that it is axially within the focal volume and sufficiently close to the focus in the transverse plane to produce a detectible peak in the OCT interferogram. The phase ϕ of the interference fringes produced by the particle is linearly dependent upon its axial position:

$$\phi(z_p, z_d) = \frac{4\pi n(z_p - z_d)}{\lambda_c} \tag{1}$$

where λ_c is the center wavelength of the light source and n the refractive index of the medium.

After axial displacement, the phase of the OCT signal is thus modified: $\Delta\phi=4\pi n\Delta z_p/\lambda_c$. One problem with using phase for sensing the displacement magnitude, however, is that if $\Delta z_p>\lambda_c/n$ then the phase must be unwrapped to properly estimate Δz. One advantage is that in the absence of phase noise, this measurement is more sensitive to small

Δz than the measurement of ΔA. It should also be noted that a particle in motion can be detected using Doppler OCT to sense the time-varying phase change $\Delta\phi/\Delta t$ which is proportional to the axial component of the particle velocity $\Delta z/\Delta t$ [20].
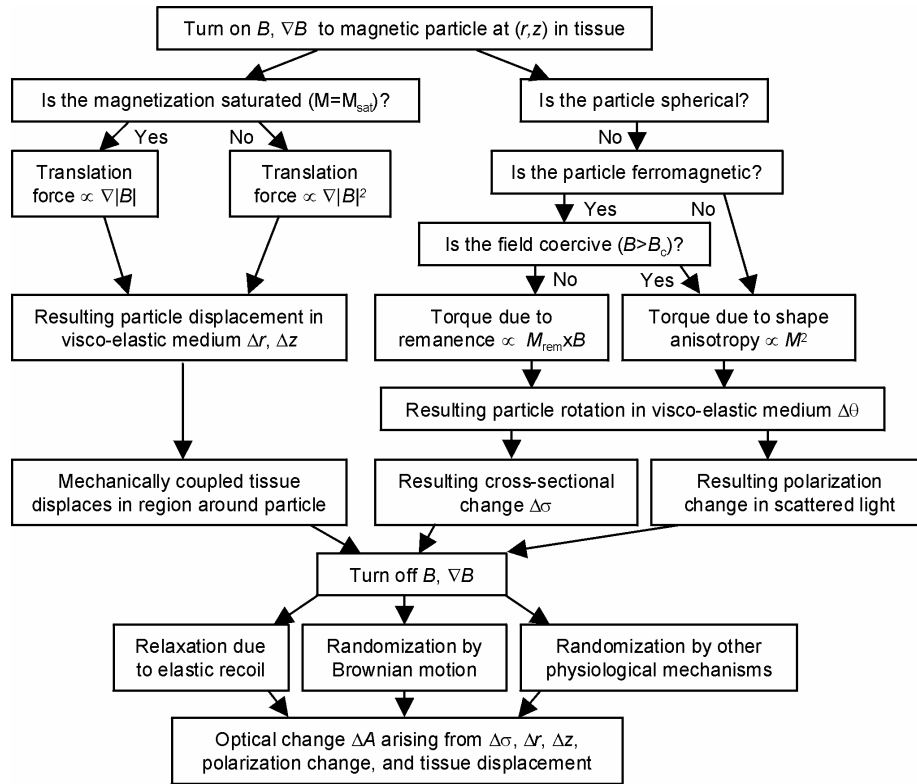

Figure 1. Flow chart illustrating relationships between the various concepts discussed below. The particle motion and optical contrast are related to the particle magnetic properties, applied magnetic field, and tissue properties.

In this work we have chosen to detect the change in the OCT signal amplitude A (measured by computing the amplitude of the complex analytic signal derived from the OCT interferogram). This is partly motivated by the difficulty in achieving phase stability between axial scans; however it also provides unambiguous measurement of the particle displacement without the need for phase unwrapping. In this situation, let us consider a low-coherence light source with a Gaussian spectral shape, a coherence length l_c, and a Gaussian transverse beam profile described by the spot radius w_0. It has been previously shown that the resulting change in the OCT signal A can be written:[15]

$$\frac{\Delta A_{max}}{A} = \sqrt{2}\sqrt{\frac{\left|\Delta\vec{r}_p\right|^2}{w_0^2} + 4\,ln\,2\frac{\Delta z_p^2}{l_c^2}} = \sqrt{2}\delta \qquad (2)$$

where ΔA_{max} is the change in the OCT signal at a spatial position which provides the maximum change (which generally occurs at the center positions of the particle before and after movement). Basically this states that ΔA is proportional to the particle displacement in a Cartesian coordinate system that is scaled by the optical resolution of the OCT system.

Now, let us consider a non-spherical particle that has rotated. The OCT amplitude A will change as a result of the changing transverse particle cross-section σ within the imaging beam. For small particles (diameter$<<w_0$), ΔA is

directly proportional to the cross-sectional area change $\Delta\sigma$. However, this is an oversimplification when considering the polarization dependence of scattering. For non-spherical particles on the size scale of the light wavelength or larger, the backscattering efficiency Q_{bs} varies significantly depending on the relative orientation of the particle and the incident polarization, which will significantly modify A.

There are other physical mechanisms for magnetically-induced polarization-dependent scattering (traditionally known as magneto-optical effects) which are relevant here. For nanoparticle agents at high densities, it may be possible to observe the Cotton-Mouton effect in which ferrofluids aggregate into linear structures along applied magnetic field lines such that a magnetically-inducible birefringence is observed.[20] A photoelastic medium which is stressed (in this case by magnetic particles) also gives rise to birefringence.[21] Polarization-sensitive OCT[22] is particularly suited to detecting these magneto-optical effects. However, a single detector OCT system is still sensitive to polarization changes in the scattered light because $A \propto \left| \left\langle p_{sample} \mid p_{reference} \right\rangle \right|^2$ where $\left| p \right\rangle$ is the light polarization state returned from each arm of the interferometer. For example, if the reference and sample arm light are both identically linearly polarized, then rotation of the sample arm polarization by θ gives rise to an amplitude change $\Delta A \propto \sin^2(\theta)$.

In the above treatment we assumed the particle dimensions were subresolution. In practice, the size of blood pool agents must be kept below ~ 5 μm for unrestricted travel through the vasculature. This maximum is nominally the same size as l_c and w_0 for many OCT systems. However, it is also interesting to note that adjacent scattering objects within the medium will displace that are mechanically coupled to the magnetic agents, such as cell membranes or organelles.

2.2. Effect of the micromechanical environment

In this subsection we relate the magnetically applied force F or torque τ to the resultant displacement or rotation of a particle and its surrounding medium.

First, consider a point magnetic particle embedded within an infinite elastic medium described by Young's modulus E and Poisson ratio v. A force $F_{z'}$ is applied along the axis z' to a particle at the origin. This concentrated force may induce plastic flow locally, but may be treated by considering the stresses applied to a larger sphere beyond which deformation is perfectly elastic.[23] The resulting displacements $\Delta r'$, $\Delta z'$ are computed from the solution to the stress function:[23]

$$\Delta r' = -\frac{F_{z'}}{8\pi E} \cdot \frac{1+v}{1-v} \cdot \frac{r'z'}{\left(r'^2 + z'^2\right)^{3/2}}$$

$$\Delta z' = \frac{F_{z'}}{8\pi E} \cdot \frac{1+v}{1-v} \cdot \frac{(3-4v)r'^2 + (4-4v)z'^2}{\left(r'^2 + z'^2\right)^{3/2}}$$

(3)

To avoid the singularity at the origin, one considers the force applied at the surface of the particle (*e.g.*, for a sphere, $r'^2 + z'^2 = d^2/4$). As expected, the resulting displacements are linear with the applied force and inversely proportional to the Young's modulus. For a typical Poisson ratio of 0.25, one finds that the axial displacement is on average much larger than the radial, by a factor of ~ 5. The magnitudes of $\Delta r'$ and $\Delta z'$ fall off approximately inversely proportional to the distance from the particle.

In order to estimate the time it takes for a particle to reach equilibrium (for imaging speed considerations), we consider the effects of viscous drag where the force (for laminar flow) $F_{drag} = -3\pi d\eta v$, where η is the viscosity of the medium and v the velocity of the particle. To simplify matters, let us consider the one-dimensional case in x' of a particle acting like a piston such that it applies a spatially invariant magnetically induced force F_b at time $t=0$ to a cylinder containing a medium with modulus E fixed at a position length L from the particle, so that the elastic force $F_{elastic} = (x'(0) - x'(t))E\pi d^2/4L$. Therefore, the equation of motion for a particle of mass m is $m\partial^2 x'/\partial t^2 = F_b + F_{drag} + F_{elastic}$, and the solution is typically that of an over-damped oscillator such that it can be approximated:

$$x'(t) = x'(0) + \frac{4F_b L}{\pi d^2 E}\left(1 - e^{-\frac{dE}{12\eta L}t}\right), \qquad m << \frac{9\eta^2 L\pi}{E} \tag{4}$$

A magnetic particle embedded in soft tissue with E=2 kPa experiences a viscosity similar to that of water (η=0.001 Pa·s), which implies that the inequality above is easily satisfied under biomechanical conditions. For example, If a distance of L=1 mm is to be measured between the particle and the fixed point within the tissue, a magnetite particle smaller than d=2 mm is needed to satisfy the inequality. In the case of a 1 μm diameter particle with an applied force of 1 pN, we find that the equilibrium displacement $x'(\infty)$-$x'(0)$=0.64 μm, and the time it takes to reach half the equilibrium displacement $t_{1/2}$ = 4.2 ms.

At this point we have assumed that the viscoelastic medium is perfectly homogeneous. However, clearly, on the size scale of a microscopic particle, the location and binding of the particle to individual cells within its environment play an important role. This is particularly true when considering rotation of ferromagnetic particles, because magnetorelaxometry measurements have shown that immobilization of magnetic nanoparticles quenches their Brownian relaxation.[24] In the limiting case where the magnetic particle is completely unbound, we can describe the particle rotation in terms of the hydrodynamic retarding torque τ_{hyd}=-$\kappa V\eta\omega$ (where κ is a shape factor, V is the hydrodynamic volume of the particle, and ω is the angular velocity), the inertial torque $I\partial\omega/\partial t$ (where I is the particle moment of inertia), and the applied magnetic torque τ_{mag}.[25] Because the form of τ_{mag} is rotationally dependent and varies with the magnetic properties of the particle, we will postpone a discussion of the dynamics of rotation to the following subsection.

2.3. Magnetic particle properties

All substances are characterized by a magnetic susceptibility χ=$\partial M/\partial H$, where M is the magnetization and H the applied magnetic field. Although χ is well-defined when M and H are nearly zero, it is not constant when M approaches saturation (M_{sat}), χ begins to saturate. Within a weakly magnetic medium ($\mu\approx\mu_0$) of χ_{med} and M_{med}, the applied magnetic field B=H/μ_0. In this medium, the force on a small magnetic particle with χ=χ_p, magnetization M_p, saturation magnetization M_{sat}, and volume V is written $\vec{F} = V\left(\left(\vec{M}_p - \vec{M}_{med}\right)\cdot\nabla\right)\vec{B}$, where it is useful to consider the following limiting cases:[26]

$$\vec{F} = \frac{V(\chi_p - \chi_{med})\nabla|\vec{B}|^2}{2\mu_0}, \qquad \left|\vec{M}_p\right| << M_{sat}$$
$$\vec{F} = VM_{sat}\nabla|\vec{B}|, \qquad\quad \left|\vec{M}_{med}\right| << \left|\vec{M}_p\right| = M_{sat} \tag{5}$$

To give a sense of perspective, a 1 μm particle with χ_p=1 and M_{sat}=500 kA/m in a one-dimensional magnetic field gradient with $\nabla|B|^2$=1 T^2/m and $\nabla|B|$=10 T/m will experience a force ranging from 0.2 pN (M_p<<M_{sat}) to 2.6 pN (M_p=M_{sat}). It is worth noting that $\vec{F}$ points in the same direction if the polarity of $\vec{B}$ is reversed.

Although ferromagnetic particles typically exhibit large susceptibilities, it is not necessary for them to be ferromagnetic to produce displacement. However, rotationally dependent contrast can only be achieved through the use of non-spherical ferromagnetic particles. Ferromagnetic substances exhibit remanence, that is, they maintain an internal magnetization M_{rem} that, in the case of anisotropic particles such as prolate ellipsoids, have lowest energy when aligned with the long axis of the particle. Uniaxial anisotropy is also desirable both for potentially larger $\Delta\sigma$ and for higher coercivity. This allows us to align the magnetic particles by applying a torque $\vec{\tau}_{mag} = V\vec{M}_{rem} \times \vec{B}$ which minimizes the cross-section σ when viewed along the magnetic flux lines. The dynamics of field-induced rotation within a viscous medium can be estimated using the equation of motion $I\partial\omega/\partial t = \tau_{mag} + \tau_{hyd}$, which yields:[25]

$$Tan\left(\frac{\theta(t)}{2}\right) = Tan\left(\frac{\theta(0)}{2}\right)e^{-\frac{\left|\vec{M}_{rem}\right|\left|\vec{B}\right|}{\kappa\eta}t}, \qquad I << \frac{\kappa^2\eta^2 V}{\left|\vec{M}_{rem}\right|\left|\vec{B}\right|} \tag{6}$$

where θ is the angle between $\vec{M}_{rem}$ and $\vec{B}$. The inequality determines whether inertia may be ignored. To take a marginal case: if a magnetite ellipsoid with an aspect ratio of 2 (major and minor axes of 2 μm and 1 μm, respectively) and M_{rem}=64 kA/m is exposed to a perpendicular 0.1 T magnetic field in water, the reorientation time $t_{1/2}$ (the period required to change θ from 90° to 45°) is approximately 1.4 μs. For more extreme cases (smaller η, larger B, etc.) the actual $t_{1/2}$ may be larger than that predicted with Eq. (10). It should also be noted that this is only valid for laminar fluid flow. Although in this example we estimate the Reynolds number to be ~1, for extremely fast translation or twisting, turbulence may play a significant role.

As ferromagnetic particles become smaller, M_{rem} decreases until, on the size scale of ~100 nm the superparamagnetic regime is reached, at which point M_{rem}=0.[26] For a superparamagnetic particle the Neel rotation time becomes so short that it responds more quickly than the particle can rotate, thus allowing the internal magnetization to be aligned without physical rotation. However, superparamagnets and paramagnets with shape anisotropy still experience a torque in the presence of a magnetic field, which can be described as $\tau_{mag}=\mu_0(N_a-N_b)VM^2\sin\theta\cos\theta$, where N_a and N_b are the demagnetizing factors along the major and minor axes of an ellipsoidal particle, respectively, and θ is the angle between the major axis and the applied field.[25] For example, a superparamagnetic particle with an aspect ratio of 2 (major and minor axes of 100 nm and 50 nm, respectively) experiencing M_{sat}=800 A/m in water should have a $t_{1/2}\approx 30$ ms. Ferromagnets also exhibit this behavior under high field conditions where $M=M_{sat}$, but in lower field situations the previous mechanism (alignment of M_{rem}) dominates.

Magnetic Pulse Sequence and Noise Normalization

There are many valid design options for sequencing the magnetic field application with the image acquisition. In one implementation[27] a lock-in amplifier was used to detect magnetic-specific modulation at 1 kHz, collecting data separately at each point within the OCT image. However, this type of imaging sequence can be prohibitively long. A faster, single measurement technique is to switch the magnetic field on and off for each successive axial scan, thus producing a measurement of ΔA by differencing the scan lines. Alternately, for extremely high frame rates, one may switch the magnetic field after successive frames, thus differencing entire image sets.

The major problem with MM-OCT is how to subtract the nonmagnetic motion that is intrinsic to the medium. This may occur, for example, due to the physiological motion such as cardiac and respiratory function, or it may occur due to Brownian motion. The simplest say to determine this tissue background signal is to simply measure it during image acquisition. This is performed here by acquiring two successive axial scans without any magnetic field (a_{off}) at times t and t+Δt, then applying the magnetic field during the acquisition of the third scan (a_{on}) at time t+2Δt. It is important that the time lapse Δt be kept the same between successive scans because the amount of deviation is essentially given by the correlation function of the tissue $\Gamma(\Delta t)$.[28] In this way one can normalize the magnetic signal:[15]

$$S(dB) = 10\log\left(\frac{\left\langle\left(a_{on}(t+2\Delta t)-a_{off}(t+\Delta t)\right)^2\right\rangle+\delta^2}{\left\langle\left(a_{off}(t+\Delta t)-a_{off}(t)\right)^2\right\rangle+\delta^2}\right) \tag{7}$$

where δ is a small offset (typically 1 bit) to avoid the poles. Note that we indicate averaging here, since it is necessary to acquire multiple measurements to achieve a reliable signal. This is employed in practice by spatial averaging; although temporal averaging is expected to provide similar results.

2.4. Imaging speed considerations

The above discussion suggests that faster imaging is desired to reduce background noise. On the other hand, the particle response will be reduced if sufficient time is not allowed for the full range of translation or rotation, (on the order of 4 ms and 1 μs, respectively) for magnetite microparticles in tissue-like media. If the MM-OCT signal is sufficiently large, the imaging time could be further reduced. However, one must consider the deleterious effects of heating as magnetic field switching frequencies become large. Hyperthermia induced by modulation of magnetic particles has been used for therapeutic purposes such as selective tissue lysing,[17] and generally found to be significant at frequencies above 100 kHz. Also, modulation at higher frequencies requires thoughtful design of the electromagnet because the inductance becomes prohibitive.

Imaging speed should also be chosen to minimize the background motion if it becomes prohibitive. For example, liquid environments have a characteristic speckle correlation time $t_{speckle}$ arising from Brownian motion and related to the density and size of the constituent scatterers. In chicken skin $t_{speckle} \approx 100$ ms.[29] Although averaging over a long time ($t \gg t_{speckle}$) is one way of reducing this background, the variance can be reduced to the shot noise limit by acquiring single measurements over a very short time, effectively freezing the background motion.

Another consequence of Brownian motion is that it acts to randomize the orientation of an unbound particle (such as a magnetic particle) on a time scale $t_B = 3\eta V/kT$ (where k is Boltzmann's constant and T is temperature), which results $t_B = 127$ ms for a 1 μm particle in water at room temperature. Also, biological movement such as cardiac function ($t \sim 1$ s) and respiration ($t \sim 6$ s) act to move tissue on longer time scales.

3. EXPERIMENTAL METHODS

The MM-OCT system and production of silicone-based tissue phantoms has been described in detail previously.[15] In brief, a single-mode fiber based OCT system was used which exhibited an optical resolution of 3μm axially and 8μm transversely in tissue and a sensitivity of –101dB. An electromagnet consisting of a water-jacketed solenoid coil was positioned immediately above the sample (without mechanical contact), the central bore allowing passage of the OCT imaging beam. Silicon tissue phantoms were doped with TiO_2 microparticles to simulate the optical properties of tissue, and incorporated a varying concentration of magnetite nanoparticles (Sigma-Aldrich, #637106, 20-30nm) added. *Xenopus laevis* African frog tadpoles (5 weeks old) were exposed to the same magnetite nanoparticles in their tank water 24 hours prior to imaging. The tadpoles were handled and cared for according to protocols approved by the Institutional Animal Care and Use Committee of the University of Illinois at Urbana-Champaign. Control tadpoles were handled identically except lacking exposure to magnetite nanoparticles. Tadpoles were anesthetized prior to imaging.

4. RESULTS

Figure 2 displays a typical OCT image acquired of a tissue phantom during the 3-pulse sequence of magnetic field modulation described above. This image was intentionally over-sampled to illustrate the small change in the speckle pattern that occurs only during every third line when the magnetic field is turned on. The displacements may be significantly smaller than the resolution of the system, yet provide sufficient ΔA to allow for magnetic-specific detection.
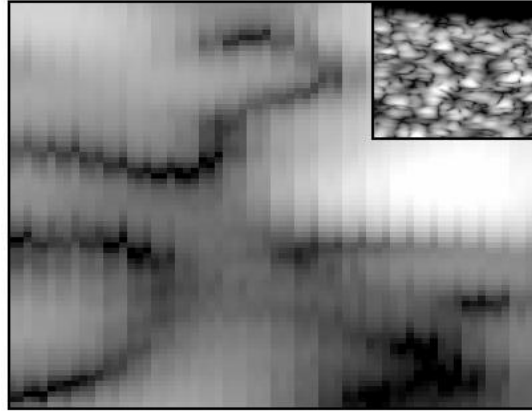
Figure 2. Closeup of an MM-OCT image (20 × 15 μm) of a tissue phantom (ρ=0.93 mg/g), inset a larger view (110 × 90 μm).[15] Image was intentionally over-sampled for illustrative purposes.

The normalized magnetic signal S (Eq. 7) was measured for a set of 8 tissue phantoms with varying nanoparticle concentrations. The results are displayed in Fig. 3. We can see that the lowest concentration providing a signal more than a standard deviation above 0dB was at 220μg/g. Statistical analysis using the T-test indicates that this concentration is detected with P>0.975 over 3 image sets (where 1 image consisted of 600 × 1000 pixels with 0.6mm × 0.7mm dimensions). However, the next two smaller concentrations studied (120μg/g and 63μg/g) repeatedly had values of S above 0dB but with variance approximately of the same size. This suggests that, although the current implementation of this system was incapable of detecting these smaller concentrations, with further improvement they may be obtainable.
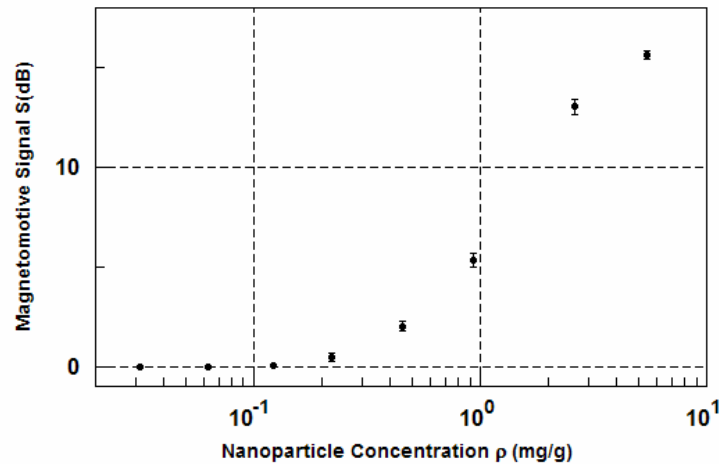

Figure 3. Plot of the MM-OCT signal S (Eq. 7) versus the concentration of magnetite nanoparticles embedded in the silicon-based tissue phantoms.

Analysis of Fig. 3 shows that the MM-OCT signal S scales approximately linearly with concentration (observing that approximately one decade change in ρ results in a decade change in S). We also investigated the scaling of the magnetomotive signal S with the magnetic field strength B and the amount of scattering in the sample. We found that the signal strength was repeatedly proportional to a power of B between 1 and 2, typically with a value of 1.5. This suggests that, according to Eq. 5, the nanoparticles are not fully saturated ($M=M_{sat}$) but in a regime close to saturation. This is supported by SQUID measurements of the nanoparticles and Teslameter measurements of the electromagnet.[15] We also found, by correlating the OCT signal with the magnetomotive signal, that the magnetomotive signal S is relatively constant with respect to the OCT signal. On one hand, highly scattering structures that are displaced will exhibit a larger ΔA than a less scattering structure displaced the same amount. However, this effect is balanced by the

equally larger background signal that is observed due to background motion. The result of this is that the depth dependence of the MM-OCT signal is proportional only to the dropoff in the magnetic field strength, and independent of the dropoff in the OCT signal. Specifically, within the tissue phantoms, we found that when the OCT signal dropped 8dB the MM-OCT signal only dropped 4dB over a depth of 0.5mm. However, this effect is limited when the OCT signal is attenuated so much as to be approximately the same magnitude as the shot noise.

Xenopus laevis African frog tadpoles were imaged after exposure to magnetite nanoparticles, which are expected to be taken up into the tadpole GI-tract through suction feeders. Figure 4 displays MM-OCT images acquired of one such tadpole from the ventral side (in the sagittal plane). Although the digestive tract is highly scattering, not permitting much optical penetration, a strong MM-OCT signal is observed on the outer surface. It is also noted that the beating heart of the tadpole (the vertically striped structure) was correctly normalized out as background motion and the resulting average MM-OCT signal in this region is no greater than background. Control tadpoles were also imaged (not shown) in the same locations, with no significant MM-OCT signal observed. There was MM-OCT signal also observed in the molding clay used to position the tadpole (upper left of Fig. 4), which is explained by observation of the tadpole excrement in this vicinity, likely containing high concentrations of nanoparticles.

Subsequent euthanization and histology of these tadpoles were performed using a Prussian blue stain to identify the locations of the nanoparticles. Slices every 100 μm were examined for signs of the magnetite, with the only positive result being obtained in the digestive tract. This is shown in Fig. 5. Control tadpoles were also examined without any evidence of the particles. In viewing Fig. 5, however, note that the melanophores lining the digestive tract are characterized by a darkly-coloring lining. Close examination of these regions revealed the absence of a Prussian-blue tint, allowing for discrimination of dark magnetite particles from melanophores and other dark tissue structures. It should be noted that the staining process may not preserve small quantities of nanoparticles which may inadvertently be rinsed from the tissue during the process. Therefore, although nanoparticles were not observed in the tadpole gills or esophagus like we might expect, the negative result is not conclusive at this time.
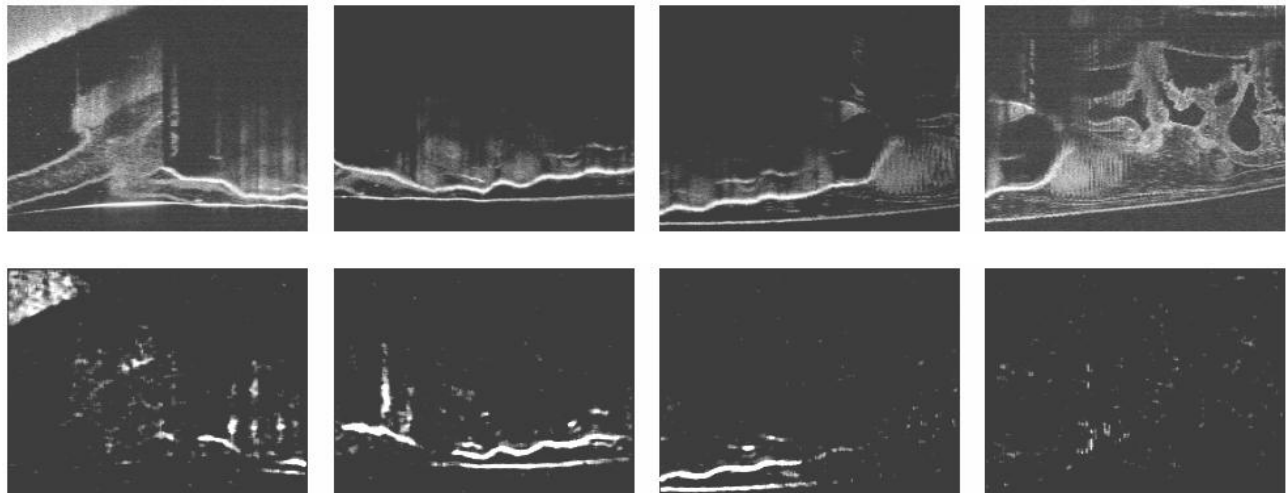

Figure 4. Images of magnetite nanoparticle-exposed *Xenopus laevis* tadpole from the dorsal side, dimensions 2 mm × 1.5 mm.[15] Top row: structural OCT images. Bottom row: MM-OCT images.
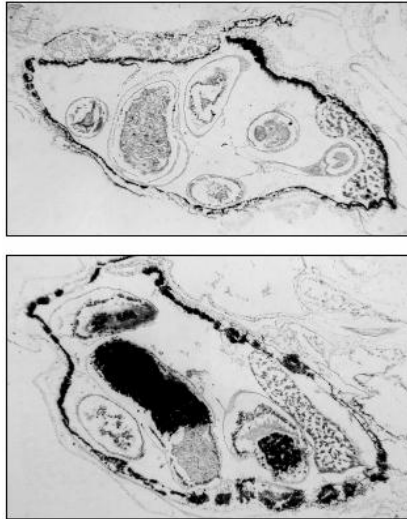
Figure 5. Histological slices of tadpoles in the region of the digestive tract, dimensions 1.6 × 1.1 mm.[15] Top: control tadpole. Bottom: magnetite-exposed tadpole. The large dark regions in the center of the magnetite tadpole digestive tract correspond to aggregated nanoparticles.

5. CONCLUSION

Magnetic nanoparticles are a promising type of probe for use in conjunction with OCT. We demonstrate theoretically a variety of mechanisms by which particle rotation or translation may be detected, either through analysis of the OCT amplitude or phase. We experimentally demonstrate this concept using a new technique called magnetomotive OCT which detects small axial displacements of magnetic nanoparticles through the change in the OCT signal amplitude. A 3-pulse sequence allows for rejection of background motion, even of highly motive structures such as the beating heart of the *Xenopus laevis* tadpole. The clear relationship between the nanoparticle concentration and the measured MM-OCT signal shows the potential for this technique for a highly-calibrated, high specificity, molecular contrast imaging system. Future work will be aimed at imaging targeted nanoparticles to provide molecular specificity. The potential for high-resolution imaging of magnetic contrast agents in conjunction with a lower-resolution whole-body modality such as MRI is an interesting area of future investigation which may provide clinicians with better tools for the diagnosis of disease.

REFERENCES

1. D. Huang, E. A. Swanson, C. P. Lin, J. S. Schuman, W. G. Stinson, W. Chang, M. R. Hee, T. Flotte, K. Gregory, C. A. Puliafito, and J. G. Fujimoto, Science **254**, 1178 (1991).
2. S. A. Boppart, A. L. Oldenburg, C. Xu, and D. L. Marks, J. of Biomed. Opt. 10(4), 41208 (2005).
3. Y. Jiang, I. Tornov, Y. Wang, and Z. Chen, Opt. Lett. **29**, 1090 (2004).
4. D. L. Marks and S. A. Boppart, Phys. Rev. Lett. **92**, 123905 (2004).
5. J. S. Bredfeldt, C. Vinegoni, D. L. Marks, and S. A. Boppart, Opt. Lett. **30**, 495 (2005).
6. U. Morgner, W. Drexler, F. X. Kartner, X. D. Li, C. Pitris, E. P. Ippen, and J. G. Fujimoto, Opt. Lett. **25**, 111 (2000).
7. T.-M. Lee, A. L. Oldenburg, S. Sitafalwalla, D. L. Marks, W. Luo, F. Jean-Jacques Toublan, K. S. Suslick, and S. A. Boppart, Opt. Lett. **28**, 1546 (2003).
8. C. Loo, A. Lin, L. Hirsch, M.-H. Lee, J. Barton, N. Halas, J. West, and R. Drezek, Technol. Cancer Res. Treat. **3**, 33 (2004).
9. J. Chen, F. Saeki, B. J. WIley, H. Cang, M. J. Cobb, Z.-Y. Li, L. Au, H. Zhang, M. B. Kimmey, X. Li and Y. Xia, Nano Lett. 5(3), 473 (2005).

10. C. Xu, J. Ye, D. L. Marks, and S. A. Boppart, Opt. Lett. **29**, 1647 (2004).
11. C. Yang, L. E. L. McGuckin, J. D. Simon, M. A. Choma, B. E. Applegate, and J. A. Izatt, Opt. Lett. **29**, 2016 (2004).
12. K. D. Rao, M. A. Choma, S. Yazdanfar, A. M. Rollins, and J. A. Izatt, Opt. Lett. **28**, 340 (2003).
13. C. Yang, M. A. Choma, L. E. Lamb, J. D. Simon, and J. A. Izatt, Opt. Lett. **29**, 1396 (2004).
14. A. L. Oldenburg, J. R. Gunther, S. A. Boppart, Opt. Lett. **30(7),** 747 (2005).
15. A. L. Oldenburg, F. Jean-Jacques Toublan, K. S. Suslick, A. Wei, and S. A. Boppart, Opt. Express **13**(17) 6597 (2005).
16. J. Schmitt, Opt. Express **3**, 199 (1998).
17. S. Hamaguchi, I. Tohnai, A. Ito, K. Mitsudo, T. Shigetomi, M. Ito, H. Honda, T. Kobayashi, M. Ueda, Cancer Sci. **94**, 834 (2003).
18. S. Palmacci, L. Josephson, United States Patent #5,262,176 (1993).
19. M. G. Harisinghani, J. Barentsz, P. F. Hahn, W. M. Deserno, S. Tabatabaei, C. Hulsbergen van de Kaa, J. de la Rosette, R. Weissleder, N. Engl. J. Med **348**, 2491 (2003).
20. C. Gross, E. Romanus, G. Glockl, P. Weber, W. Weitschies, Eur. Cell. Mater. **3** Suppl 2, 22 (2002).
21. M. M. Frocht, *Photoelasticity* (John Wiley & Sons, 1941).
22. J. F. de Boer, T. E. Milner, M. J. C. van Gemert, J. S. Nelson, Opt. Lett. **22**, 934 (1997).
23. S. Timoshenko, *Theory of Elasticity* (McGraw Hill, 1951).
24. E. Romanus, M. Huckel, C. Gross, S. Prass, W. Weitschies, R. Brauer, P. Weber, J. Magn. Magn. Mat. **252**, 387 (2002).
25. P. A. Valberg and J. P. Butler, Biophys. J. **52**, 537 (1987).
26. U. Hafeli, W. Schutt, J. Teller, M. Zborowski, *eds*, *Scientific and Clinical Applications of Magnetic Carriers*, (Plenum Press, 1997).
27. A. L. Oldenburg, J. R. Gunther, F. Jean-Jacques Toublan, D. L. Marks, K. S. Suslick, S. A. Boppart, in *Proceedings of the Conference on Lasers and Electro-Optics*, pp. 405-406 (2003).
28. J. W. Goodman, *Statistical Optics* (John Wiley & Sons, 1985).
29. G. Yao, L. V. Wang, Appl. Opt. **43**, 1320 (2004).

*Correspondence to: boppart@uiuc.edu